Synthesis Imaging in Radio Astronomy II
ASP Conference Series, Vol. 180, 1999
G. B. Taylor, C. L. Carilli, and R. A. Perley (eds.)

7. Imaging

Daniel S. Briggs
NCSA, Champaign-Urbana, IL 61801, U.S.A.

Frederic R. Schwab
National Radio Astronomy Observatory, Charlottesville, VA 22903, U.S.A

Richard A. Sramek
National Radio Astronomy Observatory, Socorro, NM 87801, U.S.A.

Abstract. This lecture covers formation of the estimated sky brightness via linear methods. The formalism of the dirty image is developed from the fundamental Fourier transform relationship between observed visibility and sky brightness. The practical computational approximation to this formalism is then covered in detail. Several weighting schemes used to control the shape of the dirty beam are presented. The convolutional gridding used to interpolate the irregularly sampled data onto a rectangular grid is examined in detail, including aliasing of sources outside the primary field of view and ramifications of the choice of convolutional gridding function.

1. Fourier Transform Imaging

A fundamental result of Lectures 1 and 2 was the existence of a Fourier transform (FT) relationship between the sky brightness I, the primary beam pattern $\mathcal{A}$, and the visibility V observed with an interferometer. From Lecture 2 (Eq. 2–26),

$$\mathcal{A}(l,m)I(l,m) = \int_{-\infty}^{\infty}\int_{-\infty}^{\infty} V(u,v)e^{2\pi i(ul+vm)}\,du\,dv\,. \qquad (7\text{–}1)$$

This simple relation holds if (a) $\left|\frac{\Delta\nu}{c}\,\mathbf{b}\cdot(\mathbf{s}-\mathbf{s_0})\right| \ll 1$ and (b) $|w(l^2+m^2)| \ll 1$. These conditions are met whenever the radiation to which the interferometer pairs respond originates in a suitably small (and confined) region of sky. Since the correction for the primary beam can be made trivially at the final stage of data processing[1] (as discussed in Lecture 1, Sec. 4.4), we shall use $I(l,m)$ to denote the *modified sky brightness*, $\mathcal{A}(l,m)I(l,m)$.

V is complex-valued and, after the usual calibration steps (see Lecture 5), is reckoned in units of flux density ('Janskys', 1 Jy = 10^{-23} ergs cm^{-2} s^{-1} Hz^{-1}), while I has units of surface brightness (flux density per unit of solid angle). A standard unit for I is Jy/beam area; sometimes Jy per square arcsecond is used instead. The units are determined by the normalization of Equation 7–1.

Equation 7–1 is used to obtain an estimate of the modified sky brightness from the observed visibilities, recorded at (u,v) points (u_k,v_k), $k = 1,\ldots,M$. In practice, M may range from ten to a few hundred with a two element interferometer, to over a million with a multi-element array like the VLA. With M

[1]This is assuming that $\mathcal{A}$ has been carefully measured over a large enough region in (l,m). Wide-field imaging, in cases in which a source covers, say, a larger region than the central lobe of the primary beam, is an especial problem. Antennas with azimuth–elevation mounts (as at the VLA) also present a problem because the primary beam patterns rotate on the sky, as functions of parallactic angle. See Lecture 6.

© Astronomical Society of the Pacific • Provided by the NASA Astrophysics Data System

modest, model fitting is feasible—and sometimes useful (see Lecture 16). But for large M the usual method of estimating I is via the discrete Fourier transform (the DFT), because extremely efficient algorithms are known for numerical evaluation of DFTs.

The topics of some of the lectures to follow also fall under the broad category of 'imaging'. But the discussion here is restricted to 'simple-minded' methods of estimating the sky brightness: that is, *directly* approximating the right-hand side of Equation 7–1, via only *linear* operations. The so-called 'dirty image' that results is a discrete approximation to I^D, where (from Lecture 1, Eq. 1–10)

$$I^D(l,m) \equiv \int_{-\infty}^{\infty}\int_{-\infty}^{\infty} S(u,v)V'(u,v)e^{2\pi i(ul+vm)}\,du\,dv\,. \tag{7–2}$$

Here, S denotes the (u,v) sampling function and V' the observed visibility; the prime indicates that the visibility data are noise-corrupted measurements. (For conciseness, I^D has been left unprimed, but it too is noise-corrupted whenever V is.)

1.1. The 'direct Fourier transform' and the FFT

Either of two methods is commonly used to numerically approximate the Fourier transform in Equation 7–2. The first, called the 'direct Fourier transform' method,[2] approximates $I^D(l,m)$ by brute-force evaluation of the sum

$$\frac{1}{M}\sum_{k=1}^{M} V'(u_k,v_k)e^{2\pi i(u_k l+v_k m)}\,. \tag{7–3}$$

If this 'direct Fourier transform' is evaluated at every point of an $N \times N$ grid, the number of real multiplications required is $4MN^2$ (the number is halved, though, assuming Hermitian data). In practice M is usually of the same order as N^2, so the number of multiplications goes roughly as N^4. The number of sine and cosine evaluations required is also $\mathcal{O}(N^4)$, as is the number of additions/subtractions.

The second method requires interpolating the data onto a rectangular grid, so that a fast Fourier transform (FFT) algorithm can be used. The process of interpolation is referred to as *gridding*. (Gridding may require sorting the

---

[2]This choice of terminology is unfortunate. The natural abbreviation for the term—'DFT'—is used almost universally (by everyone except radio astronomers) to stand for something else: the 'discrete Fourier transform'. For example, the 2-D discrete FT of an $M \times N$ matrix (x_{ij}) is the $M \times N$ matrix (y_{kl}) given by

$$y_{kl} = \sum_{p=1}^{M}\left(e^{2\pi i(p-1)(k-1)/M}\sum_{q=1}^{N} x_{pq}e^{2\pi i(q-1)(l-1)/N}\right)\,.$$

The major distinction between the two usages is that in one case the data are regularly spaced, and in the other they are not. Also, the 'direct FT' is generally not invertible, whereas the 'discrete FT' is; usually the term 'transform' is reserved for invertible transformations.

© Astronomical Society of the Pacific • Provided by the NASA Astrophysics Data System

data into order of decreasing $|u|$ or decreasing $|v|$.) The number of elementary arithmetic operations required by the technique most often used for gridding is $\mathcal{O}(M)$. The number of such operations required by an FFT algorithm (say, the Cooley–Tukey algorithm) is only a few times $N^2 \log_2 N$—not $\mathcal{O}(N^4)$! This saves much computing time for large databases, and large N especially, if an economical method of interpolation is used. However, for making small images (i.e., for N small) from small databases (M small), the 'direct Fourier transform' may be faster than the combination of gridding and FFT.

In the following sections we first discuss weighting and selection of (u, v) data and how it affects the resulting images. This applies no matter how the Fourier transform is approximated. Then we touch upon the problems that are introduced by gridding the data to permit use of the FFT—the problems of aliasing and correction for gridding.

2. The Sampling Function, and Weighting the Visibility Data

The sampling function S and its Fourier transform, the synthesized beam B, were introduced in Lecture 1. In practice the data are variously weighted, according to their reliability and to control the shape of the synthesized beam.

2.1. The sampling function

S is a 'generalized function', or 'distribution', which may be expressed in terms of the two-dimensional Dirac delta function, or 'δ-distribution',

$$S(u,v) = \sum_{k=1}^{M} \delta(u - u_k, v - v_k)\,. \tag{7–4}$$

It is useful to introduce a second generalized function, called the *sampled visibility function* or, alternatively, the (u, v) *measurement distribution*,[3]

$$V^S(u,v) \equiv \sum_{k=1}^{M} \delta(u - u_k, v - v_k) V'(u_k, v_k)\,. \tag{7–5}$$

That is, $V^S = SV'$. Let $\mathfrak{F}$ denote the Fourier transform operator. Equation 7–2 can be rewritten

$$I^D = \mathfrak{F}V^S = \mathfrak{F}(SV')\,. \tag{7–6}$$

By the *convolution theorem*, which says that the Fourier transform of a product of functions is the convolution of their FTs (see, e.g., Bracewell 1978),

$$I^D = \mathfrak{F}S * \mathfrak{F}V'\,, \tag{7–7}$$

[3]Note that the visibility measurements are not, in actuality, point samples of the inverse Fourier transform of the modified sky brightness $\mathcal{A}I$, but that instead they represent *local averages* of it. Time- and frequency-averaging, which are discussed in Lecture 2, are the dominant averaging effects. One should try to choose observing parameters (integration time and bandwidth) that make relatively safe our assumption here about δ-function sampling. This matter is further discussed in Lectures 17 and 18.

© Astronomical Society of the Pacific • Provided by the NASA Astrophysics Data System

where $*$ denotes convolution. For a point source of unit strength, centered at position (l_0, m_0), $|V'(u,v)| \equiv 1$ (plus noise), and $\mathfrak{F}V'$ is the (shifted) Dirac δ-function: $\mathfrak{F}V'(l,m) = \delta(l - l_0, m - m_0)$. So the point source response of the array, i.e., the *synthesized beam*, is given by $B = \mathfrak{F}S * \delta = \mathfrak{F}S$. Equation 7–7 is the familiar result (Lecture 1, Eq. 1–11) that the observed brightness is the true brightness convolved with this 'beam'.

It should be apparent that the so-called 'direct Fourier transform', as defined by Equation 7–3, is *exactly* I^D. That is to say, that—assuming δ-function sampling—$I^D(l,m)$, as defined by Equation 7–2, is given exactly by the discrete summation Eq. 7–3. Equation 7–7 holds exactly for the 'direct Fourier transform' method, (an analogous relation is given below for the FFT method). Of course, a computed 'direct Fourier transform' image is indeed an approximation, but only in the sense that it is inevitably a discretely sampled version of I^D and that the sums are computed in finite precision arithmetic.

2.2. Weighting functions for control of the beam shape

In analogy to Equation 7–4, a *weighted sampling function*, or *weighted sampling distribution*, can be written as

$$W(u,v) = \sum_{k=1}^{M} R_k T_k D_k \delta(u - u_k, v - v_k)\,. \tag{7–8}$$

And, in analogy to Equation 7–5, one can define a *weighted, sampled visibility function*, or *weighted and sampled measurement distribution*, V^W according to $V^W = WV'$, or, explicitly,

$$V^W(u,v) = \sum_{k=1}^{M} R_k T_k D_k \delta(u - u_k, v - v_k) V'(u_k, v_k)\,. \tag{7–9}$$

The coefficients R_k, T_k, and D_k (discussed below) are weights assigned the visibility points. These data points may represent time-averages of visibility measurements spaced along the loci of the (u,v) tracks. R_k is a weight that indicates the reliability of the k^{th} visibility datum. It may depend on the integration time, the system temperature, and the bandwidth used for that data point.

There is no control over the value of R_k in the image formation, and one might hope to ignore it here. Yet the manner in which the data samples are combined will influence the sensitivity of the final map as discussed in Lecture 8. It is an unfortunate reality that the data weighting which produces the most desirable beam from an imaging standpoint will often utilize the data very irregularly and result in poor sensitivity—the subjects of imaging and sensitivity are inextricably linked. The procedure for best balancing the desirable properties of low & uniform sidelobes, high resolution, and high sensitivity for a given project is complicated and still somewhat heuristic, though some progress has been made towards reasonable compromises that work well in the majority of cases. Here we present several examples showing the effect of different parameters on the weighting, but be aware that the best strategy for a given project may use more than one in combination. See Briggs (1995) for a more exhaustive treatment of different weighting strategies.

© Astronomical Society of the Pacific • Provided by the NASA Astrophysics Data System

The full data calibration may not be available at the imaging stage, but it is often the case that the thermal variation of the data sample is the dominant contribution to R_k or that the non-random components of R_k can be ignored. In this case, it can be assumed that R_k is proportional to the inverse variance of the sample distributions of $\mathrm{Re}\, V'_k$ and $\mathrm{Im}\, V'_k$. The factor by which the point source sensitivity of the output dirty map is degraded by the choice of the T_k and D_k can then be calculated. This has been called the weighting noise or the normalized thermal RMS, and is given by

$$WT_{\mathrm{noise}} = \Delta I^D / \Delta I^D_{\mathrm{best}} = \sqrt{\left(\sum_{k=1}^{M} T_k^2 D_k^2 R_k\right)\left(\sum_{j=1}^{M} R_j\right)} \Big/ \sum_{i=1}^{M} T_i D_i R_i \quad (7\text{–}10)$$

See Lecture 8 or Briggs (1995) for the full derivation. Modern imaging programs now often display this quantity, giving the careful user quantitative feedback about the effect of the weighting on sensitivity.

If S were a smooth, well-behaved function—say, a Gaussian—then B would have no sidelobes, just smooth 'wings'. In practice, S is a linear combination of many δ-functions, often with gaps in the (u, v) coverage corresponding to missing interferometer spacings. There is always a finite limit to the extent of the (u, v) coverage, corresponding to the largest (projected) spacing of interferometer elements. In addition, for most arrays more data points fall in the inner region of the (u, v) plane than further out. This tends to give higher weight to the low spatial frequencies. Thus the natural sampling may impair effective deconvolution or mask interesting features of I. All of these real world concerns combine to produce a beam which is rarely what the astronomer wishes. The density weight D_k and the taper T_k are completely arbitrary and can be specified in many Fourier transform imaging programs, to 'fine-tune' the beam shape and combat the natural sampling as best possible. They are factored into two independent functions purely for convenience in specification. The T_k are used to downweight the data at the outer edge of the (u, v) coverage, and thus to suppress small-scale sidelobes and increase the beamwidth. The D_k are used to offset the high concentration of (u, v) tracks near the center, and to lessen the sidelobes caused by gaps in the coverage; i.e., to simulate more uniform (u, v) coverage. We shall discuss these forms of weighting separately.

The tapering function The T_k are specified by a smooth function T: $T_k = T(u_k, v_k)$. T is usually separable, so that $T(u, v) = T_1(u)T_2(v)$; and often it is a radial function (i.e., a function with circular symmetry): $T_k = T(r_k)$ where $r_k \equiv \sqrt{u_k^2 + v_k^2}$. Although functions whose radial profiles follow a power-law or powers of a cosine are occasionally used, the most prevalent form is the Gaussian. The dispersion, or the half-width at half amplitude, or the half-width at 0.30 amplitude are used in different data reduction programs to specify the characteristic width (or widths) of T (see Fig. 7–1). The modern trend has been towards specification of the taper by the equivalent convolution with a Gaussian function in the image plane, so Fig. 7–1 also gives a short table of conversions between the two conventions.

For a Gaussian taper, $T(r) = \exp(-r^2/2\sigma^2)$, the half-power beamwidth (i.e., the width of the synthesized beam, measured between half-amplitude points)

© Astronomical Society of the Pacific • Provided by the NASA Astrophysics Data System

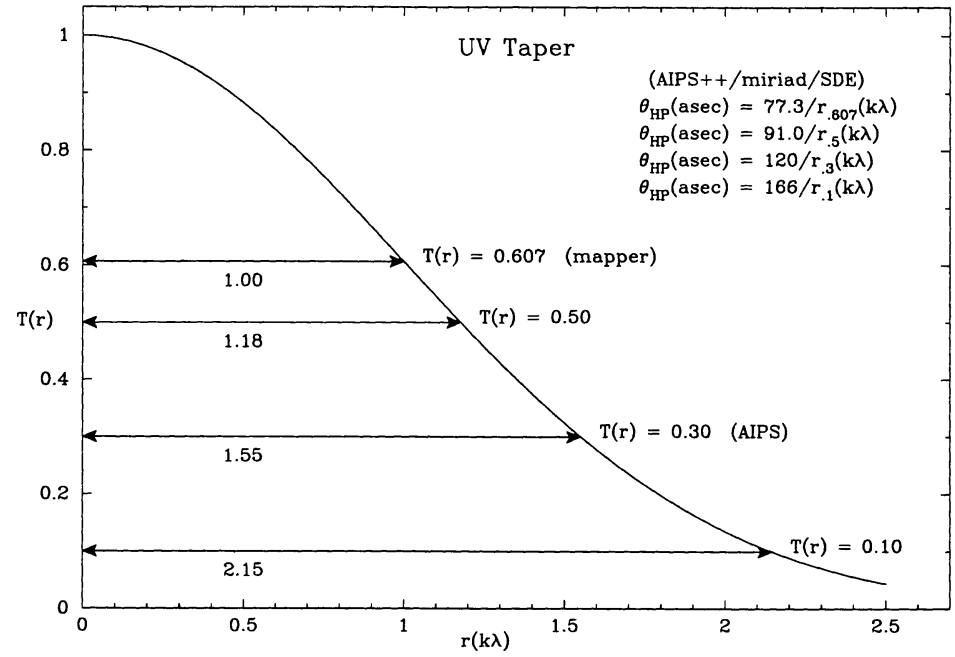

Figure 7–1. A Gaussian (u, v) taper with dispersion $\sigma = 1$ km.

is $\theta_{\rm HPBW} = 0.37/\sigma$ with θ in radians and σ in wavelengths. Translated into common units, $\theta_{\rm HPBW} = 0.77\lambda_{\rm (cm)}/\sigma_{\rm (km)}$ arcseconds. This holds only for a densely sampled Gaussian that is not truncated by the edge of the (u, v) coverage. When the taper is negligible at the edge of the (u, v) coverage (assuming dense coverage), one can use a filled circular aperture approximation, for which $\theta_{\rm HPBW} = 2.0\lambda_{\rm (cm)}/a_{\rm (km)}$ arcseconds, where a is the radius of the aperture. Real-life observational geometries and (u, v) coverages often produce larger $\theta_{\rm HPBW}$ and, frequently, elongated beams. Examples of the VLA point source response with different (u, v) tapers are shown in Figure 7–2.

Instead of de-emphasizing data near the outer boundary of the (u, v) coverage, it is sometimes desirable to downweight the data near $u = v = 0$. An undersampled large-scale emission region may introduce large undulations in image intensity that are hard to remove. These can present a problem for detecting a weak point source embedded within a region containing extended emission. Minimum (u, v) limits and other forms of downweighting are often used to diminish the effect of these low spatial frequency data points.

Finally, while one normally thinks of tapering as downweighting the visibility data as a function of radius, it is also possible to inverse taper and upweight the higher spatial frequencies instead. An upweighting has no equivalent finite convolution in the image plane, but it can arise in the solution of a convolution equation between two Gaussians. If one wishes to form a Gaussian beam of a given shape—say for matching resolution between images of an object at two epochs—one can solve the equation $B_{\rm target} = \mathit{taper} * B$ for the equivalent taper in the visibility plane. This might involve an inverse taper, but can still yield reasonable results if the upweighting is not too severe. Unfortunately, few imaging programs are able to do this yet, but the capability will likely become more

© Astronomical Society of the Pacific • Provided by the NASA Astrophysics Data System

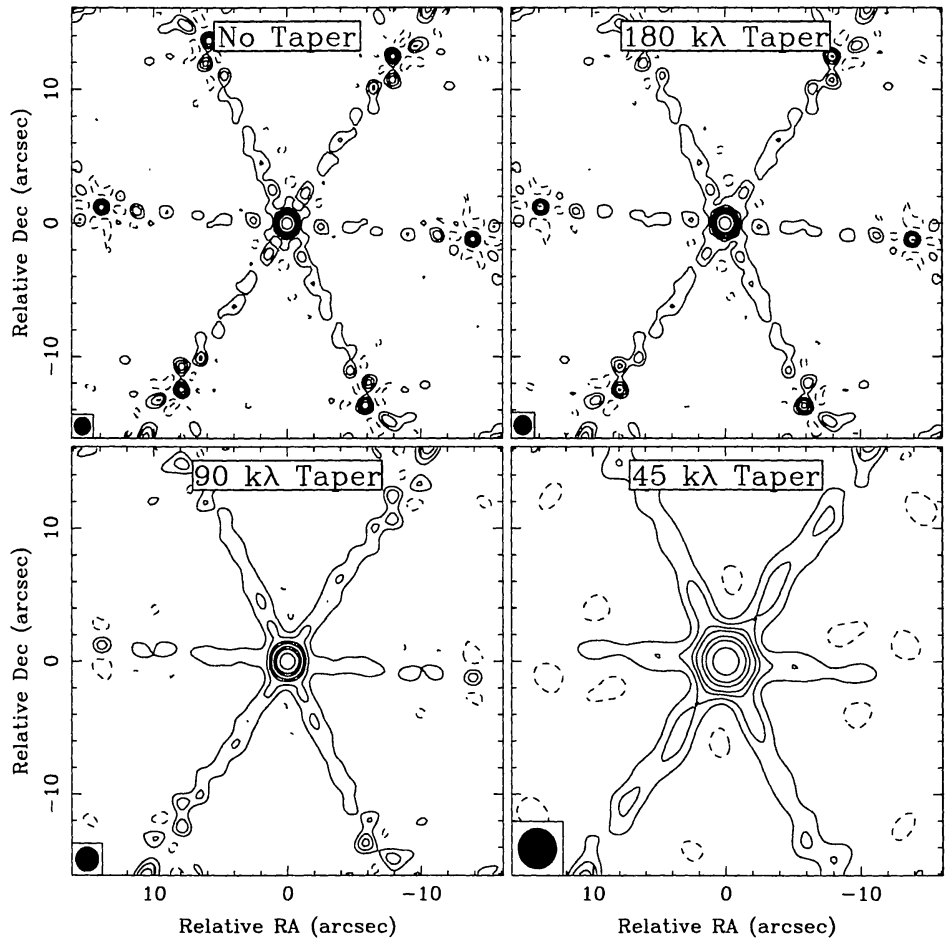

Figure 7–2. The effect of a Gaussian taper on the point source response of a VLA snapshot in the **A** configuration at 20-cm wavelength. As a narrower Gaussian taper (i.e., a heavier tapering) is applied, the half-power width of the point spread function increases and the inner sidelobes are reduced.

common in the future. Details of this formalism are given in Appendices B–D of Briggs 95.

The density weighting function: The density weighting function can be used to compensate for the clumping of data in the (u, v) plane by weighting by the reciprocal of the local data density. Two choices for this weighting are commonly provided:

$$D_k = 1\,, \qquad \text{called } \textit{natural weighting}, \tag{7–11}$$

$$\text{and} \quad D_k = \frac{1}{N_s(k)}\,, \qquad \text{called } \textit{uniform weighting}, \tag{7–12}$$

where $N_s(k)$ is the number of data points within a symmetric region of the (u, v) plane, of characteristic width s, centered on the k^{th} data point. (s might be the radius of a circle or the width of a square.)

Natural weighting, with all points treated alike, gives the best signal-to-noise ratio for detecting weak sources. However, since the (u, v) tracks tend

© Astronomical Society of the Pacific • Provided by the NASA Astrophysics Data System

to spend more time per unit area near the (u, v) origin, natural weighting emphasizes the data from the short spacings, and tends to produce a beam with a broad, low-level plateau. This latter feature is especially undesirable when imaging sources with both large-scale and small-scale structure.

With uniform weighting, a common choice for N_s is to count all the points that lie within a rectangular block of grid cells in the neighborhood of the k^{th} datum (gridding is discussed later).[4] This produces a beam specified largely by the tapering function T. In the case where different points have different reliability weights R_k, the $N_s(k)$ is usually replaced by the total reliability weightsum in that same region. In most Fourier transform imaging programs s is a free parameter selected by the user. The default value of s is usually a function of the physical image dimension, so by merely changing the image or pixel size, one is also changing the uniform density weights.

Sometimes, especially in the VLA 'snapshot' mode of observing, uniform weighting may not be 'uniform' enough. Although all cells have equal weight, the filled cells are still concentrated toward the center and along the arms of the VLA 'Y'. At the further expense of signal-to-noise ratio, the size parameter s can be increased. This 'super-uniform weighting' gives lightly sampled, isolated cells weights comparable to those given cells in well-sampled parts of the plane. The result is again a beam shape controlled more by the tapering function and less by the arrangement of the sampled visibilities. Examples of the VLA point source response obtained with various weighting functions are shown in Figure 7–3.

A hybrid form of the uniform and natural weighting called *robust weighting* has recently been introduced, which arises from a minimization of the summed sidelobe power and thermal noise. A typical tradeoff between beam resolution and weighting noise for a full track VLA observation, traced by varying the robustness parameter, is shown in Figure 7–4. Characteristically this tradeoff curve is an 'L' shape, meaning that one can profitably work either in the knee of the curve for a compromise beam with intermediate properties in both parameters, or work on one leg of the 'L' and slightly improve one parameter without greatly affecting the other. This weighting scheme is currently available in most packages and is discussed extensively in Chapter 3 of Briggs (1995). As with the other weighting parameters described, the most appropriate robustness parameter for a given dataset must be determined empirically.

3. Gridding the Visibility Data

To take advantage of the extreme efficiency of the FFT algorithm, visibility values must be assigned to a regular, rectangular matrix or 'grid', usually with a power-of-two number of points along each side. Since the observed data seldom lie on such a grid, some procedure (an interpolation procedure comes most readily to mind) must be used to assign visibility values at the grid points, based on

[4]In the AIPS implementation, these blocks are called 'uniform weight boxes', and the size of the weight box determines the degree of super-uniform weighting. In AIPS++/miriad/SDE, super-uniform weighting is specified with a Field of View (FOV) parameter. In most respects, an AIPS box size of N is equivalent to an FOV of 1/N.

© Astronomical Society of the Pacific • Provided by the NASA Astrophysics Data System

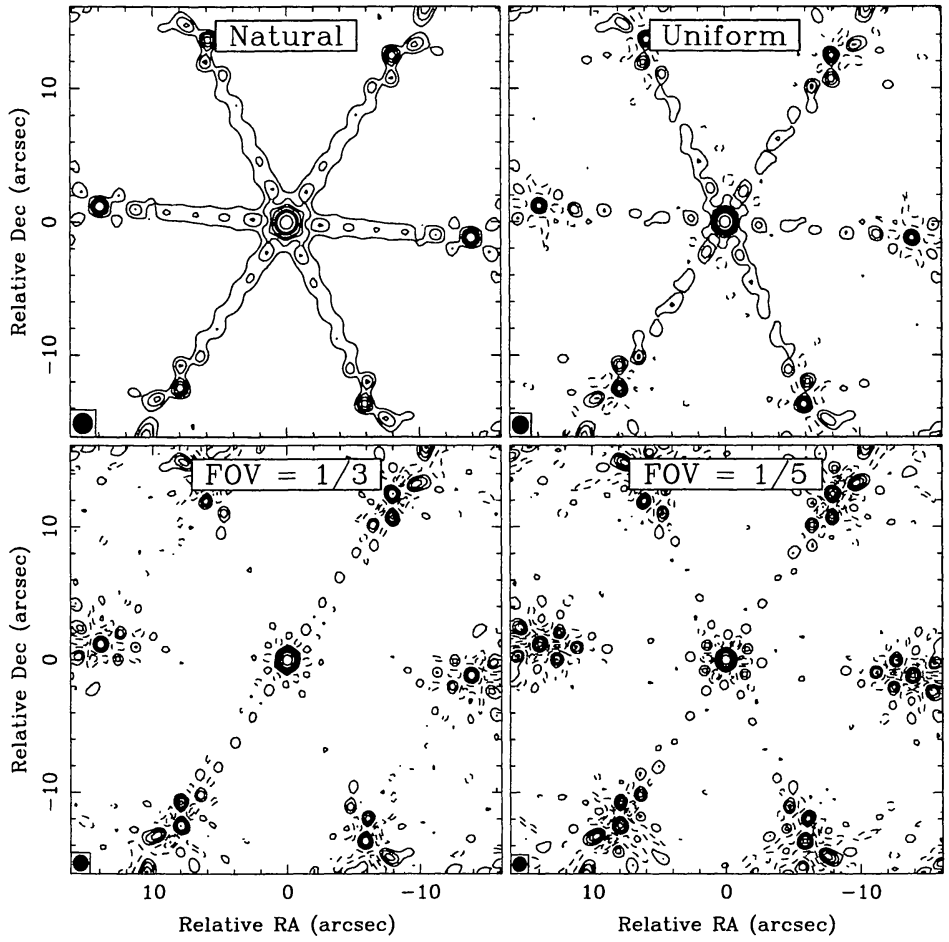

Figure 7–3. The effect of different weighting functions on a VLA 'snapshot' image of a point source.

the observed values.[5] There are many ways to achieve this interpolation (see, e.g., Thompson & Bracewell 1974), but with quasi-randomly placed observations a convolutional procedure in the (u, v) plane leads to an image with predictable distortions and to results that are easy to visualize. Convolution is not, in fact, a pure interpolation procedure, since it combines smoothing, or averaging, with interpolation. This should not be viewed as undesirable—given that there often are many noisy, possibly discrepant, data points in the neighborhood of a given grid point.

3.1. Gridding by convolution

The idea is to convolve the weighted, sampled measurement distribution V^W with some suitably chosen function C, and to sample this convolution at the

[5]Some special array geometries (e.g., 'T's and Crosses, with elements aligned linearly N–S and E–W) can provide regularly spaced data. See, for example, the description of the Clark Lake array by Erickson *et al.* (1982). The assumption (mentioned below) of a sufficiently large number of data points in the neighborhood of each filled 'cell' is not required. However aliasing problems persist, because of the regular sampling.

© Astronomical Society of the Pacific • Provided by the NASA Astrophysics Data System

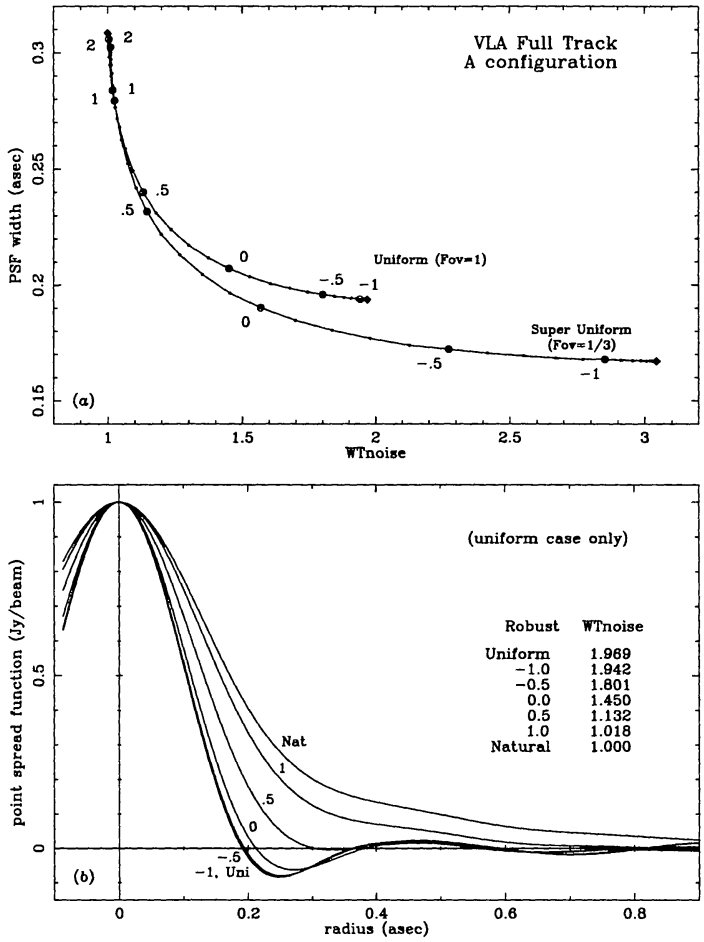

Figure 7–4. The effect of robustness parameter on weighting noise and beam shape for a full track VLA observation. The Uniform and Robust=−1 traces in panel **(b)**, are visually identical, with the Robust=−.5 trace just above them. Notice that all plotted traces are distinct in WTnoise, however.

center of each 'cell' of the grid. For economy's sake—and because it seems reasonable for the value assigned at a given grid point to equal some local average of the measurements—C, in practice, is always taken to be identically zero outside some small, bounded region A_C. Since V^W is a linear combination of M δ-functions, this convolution $C * V^W$, evaluated at the grid point (u_c, v_c), is given by

$$\sum_{k=1}^{M} C(u_c - u_k, v_c - v_k) V^W(u_k, v_k) . \tag{7–13}$$

Note that, since the region A_C is quite small in area, there are generally *many* fewer than M nonzero terms in this sum.

Note also that Eq. 7–13 does not, in fact, represent a *local average* of the measurements in the neighborhood of (u_c, v_c). For that, some sort of normalization would be required—say, multiplication by the area of A_C, followed by division by the number of data points whose shifted coordinates $(u_c - u_k, v_c - v_k)$ lie within the region A_C (and one would want C to integrate to unity). When this

© Astronomical Society of the Pacific • Provided by the NASA Astrophysics Data System

particular form of normalization is used, the normalized sum (ignoring weighting) approaches the *non-discrete, integral convolution* $C*V$ evaluated at (u_c, v_c) as the number of measurements increases without bound, provided that the measurements in the neighborhood of (u_c, v_c) are uniformly distributed, and provided that the noise in V' is well-behaved. In practice, this straightforward form of normalization is not always incorporated in imaging—so the matter of normalization becomes intertwined with that of 'density weighting', discussed above.

The operation of sampling $C * V^W$ at all points of the grid may be represented by the equation

$$V^R = R\left(C * V^W\right) = R\left(C * (WV')\right), \tag{7-14}$$

where (as usual) multiplication is indicated by juxtaposition and where R, a 'bed of nails' resampling function, is given in terms of Bracewell's 'sha' function (denoted III) by

$$R(u,v) = \text{III}(u/\Delta u, v/\Delta v) = \sum_{j=-\infty}^{\infty} \sum_{k=-\infty}^{\infty} \delta(j - u/\Delta u, k - v/\Delta v)\,. \tag{7-15}$$

Here, Δu and Δv define the cell size—i.e., the separation between grid points. This operation is called *resampling* (hence the R-notation) because, as you recall, the interferometer array earlier provided the samples embodied in V^S and V^W. Now, since V^R is a linear combination of regularly spaced δ-functions, a matrix of samples of its Fourier transform $\mathfrak{F}V^R$ can be obtained by a discrete Fourier transform. Thus $\mathfrak{F}V^R$ can be calculated by the FFT algorithm.

$\mathfrak{F}V^R$—after normalization, and after one simple correction—is what you have been seeking: a 'dirty' image—a cheap approximation to I^D. Denote $\mathfrak{F}V^R$ by $\widetilde{I}^D$.

Applying the convolution theorem to Equation 7–14, $\widetilde{I}^D$ is given by

$$\widetilde{I}^D = \mathfrak{F}R * \left[(\mathfrak{F}C)\left(\mathfrak{F}V^W\right)\right] = \mathfrak{F}R * \left[(\mathfrak{F}C)\left(\mathfrak{F}W * \mathfrak{F}V'\right)\right]\,. \tag{7-16}$$

(Please refer now to Fig. 7–5 for a graphical interpretation of Eq. 7–16 and for an illustration of the operations that are described in the remainder of this section.) III is its own Fourier transform; R behaves similarly—by the dilation property of the FT (see Sec. 4.1.),

$$(\mathfrak{F}R)(l,m) = \Delta u\,\Delta v \text{III}(l\Delta u, m\Delta v) = \Delta u\,\Delta v \sum_{j=-\infty}^{\infty} \sum_{k=-\infty}^{\infty} \delta(j - l\Delta u, k - m\Delta v)\,. \tag{7-17}$$

One effect of the resampling is to make $\widetilde{I}^D$ a periodic function of l and m, of period $1/\Delta u$ in l and period $1/\Delta v$ in m. Another effect, called *aliasing*, is also introduced. It, too, arises because of the convolution with the scaled sha function $\mathfrak{F}R$ (more on this later, in Sec. 3.2.).

The FFT algorithm generates one period of (a discrete version of) $\widetilde{I}^D$. To image a rectangular region of width $N_l\Delta\theta_l$ radians in l and $N_m\Delta\theta_m$ in m, one

© Astronomical Society of the Pacific • Provided by the NASA Astrophysics Data System

chooses grid spacings satisfying $N_l \Delta u = 1/\Delta\theta_l$ and $N_m \Delta v = 1/\Delta\theta_m$ wavelengths. An $N_m \times N_l$ FFT yields the discretely sampled version of $\widetilde{I}^D$. Let P denote the region over which $\widetilde{I}^D$ is computed— i.e., P, which is called the *primary field of view*, is given by $|l| < N_l \Delta\theta_l/2$, $|m| < N_m \Delta\theta_m/2$.

The net effect of the gridding convolution is to multiply the sky brightness by a function $c(l,m)$, the FT of the convolving function C (i.e., $c \equiv \mathfrak{F}C$). The tapering function T, introduced earlier for control of the beam shape, has the effect of a convolution in the image domain.

An image representing the point source response of the array, or the 'dirty beam' B^D, can be obtained by setting all the measurements $V'(u_k, v_k)$ to unity and following the steps outlined above. Denote the image so obtained by $\widetilde{B}^D$.

Normally, $\widetilde{I}^D$ and $\widetilde{B}^D$ are corrected for the effect of the gridding convolution by pointwise division by c: The so-called 'grid-corrected' image is given by

$$\widetilde{I}^D_c(l,m) = \frac{\mathfrak{F}R * [(\mathfrak{F}C)\,(\mathfrak{F}V^W)]}{\mathfrak{F}C} = \frac{\widetilde{I}^D(l,m)}{c(l,m)}\,, \tag{7–18}$$

and the 'grid-corrected' beam by

$$\widetilde{B}^D_c(l,m) = \frac{\widetilde{B}^D(l,m)}{c(l,m)}\,. \tag{7–19}$$

The commonly used term 'grid corrected' is, in a way, a misnomer, since one is actually correcting for the effect of the convolution function C. The grid correction is not an exact correction, except in the limit of a large number of well-distributed visibility measurements. It also is not exact due to the presence of R in Equation 7–14 and $\mathfrak{F}R$ in Equation 7–16. It could be so only if $c(l,m)$ were identically zero outside of the region being imaged; this is impossible because C is confined to a bounded region A_C.[6]

Finally, $\widetilde{I}^D_c$ and $\widetilde{B}^D_c$ both are normalized by a scaling factor selected so that the peak of $\widetilde{B}^D_c$ is of unit flux density. One may as well not alter the notation to reflect this, since it is a trivial operation.

If $c(l,m)$ tends sufficiently rapidly to zero outside P, so that the resampling can be ignored, and if the (u,v) samples are well enough distributed for the gridding correction to be approximately valid, then $\widetilde{I}^D_c$ is a good approximation to I^D— that is, Equation 7–16 becomes

$$\widetilde{I}^D_c = \mathfrak{F}W * \mathfrak{F}V'\,, \tag{7–20}$$

—and then the usual convolution relation between I^D, B, and I is approximately valid with $\widetilde{I}^D_c$ and $\widetilde{B}^D_c$ substituted for I^D and B, respectively. Note, however,

[6]The FT of any nontrivial (i.e., nonzero) function which is confined to a bounded region has features extending to infinity. By a theorem of Paley and Wiener (see, e.g., Dym & McKean 1972) the FT of such a function is extremely well-behaved, in the sense that it can be analytically extended to an entire function in the complex domain (i.e., in the case of 2 dimensions, from $\mathbf{R}^2$ to $\mathbf{C}^2$). In particular, the FT cannot vanish over any open set (this is why the synthesized beam has sidelobes that 'never go away').

© Astronomical Society of the Pacific • Provided by the NASA Astrophysics Data System

that $\widetilde{B}_c^D$ is usually computed only over a region of the same dimensions as the image $\widetilde{I}_c^D$. For this reason, the deconvolution algorithms (described in Lecture 8) usually operate just on a region with one-quarter the area of the input image.

Figure 7–5 *(pp. 140–141).* A graphical illustration of the steps in the imaging process is shown in this one-dimensional example. At the top, in panels **(a)** and **(b)**, a model source and its visibility are displayed side-by-side; the results of successive imaging operations are displayed vertically. The image domain is shown on the left, and the visibility domain on the right. Horizontally opposed panels represent Fourier transform pairs. The units on the vertical axes were chosen arbitrarily— i.e., we have not bothered with normalization. The horizontal axes are in radians for the image domain plots, at left; the baselines are expressed in wavelengths for the visibility domain plots, at right.

The model source, shown in panel **(a)**, is the sum of a Gaussian-shaped extended source and four symmetrically placed point sources. The total flux density of the Gaussian is 1.5 times the sum of the fluxes in the point sources. This symmetry was chosen to ensure that the visibility function, shown in panel **(b)**, is real-valued and even, allowing a simpler display. Panel **(d)** shows the telescope transfer function, or sampling function S, which includes a central 'hole'. We have chosen a smooth function for simplicity, but one should note that no array would in fact produce a smooth sampling function. In reality, S is a sea of closely- and irregularly-spaced δ-functions, as in Equation 7–8. The triangular sampling density was chosen to mimic the fall-off in the density of samples with increasing spacing. The telescope beam B corresponding to **(d)** is shown in panel **(c)**. The data available for imaging are shown in panel **(f)**; this product of the true visibility function and the sampling function corresponds to V^S, as defined by Equation 7–9. The image which a direct transformation of **(f)** would yield is shown in panel **(e)**. This image is equal to the convolution of the beam **(c)** with the true sky brightness **(a)**. This image shows a large amplitude oscillation, reaching a negative peak centered on the position of the extended source. This effect, which is of much larger amplitude than the oscillation seen in **(c)**, is due to the missing central spacings in the (u, v) sampling and to the fact that the visibility of an extended source is relatively highly concentrated near $u = v = 0$. With sufficient computing resources (mammoth resources would often be required), one might use the 'direct Fourier transform' method of Section 1.1.; **(e)** is the image that would result.

Extra steps are required to make use of the FFT: First, the data are convolved with some suitably chosen function, and then they are resampled over a regularly-spaced grid (in practice the convolution is evaluated only at the grid points). For illustration, a simple, and crude, convolution function C was employed, as shown in **(h)**. The sharp drop-off in C creates large, oscillating wings in its Fourier transform, shown in **(g)** (the image-plane representation of the 'grid-correction function'). The data, after convolution, are shown in panel **(j)**. If a (continuous) Fourier transform were applied at this stage, the result would appear as in panel **(i)**. The important effect to note is that the outermost point sources have been inverted in amplitude. This occurs because the convolution function that we have chosen is too wide. The inner point sources have been slightly reduced in amplitude, though not inverted in sign. As the FFT requires regularly spaced data, the data in **(j)** must be sampled. The (re-)sampling function R is shown in panel **(l)**, and its transform, the replication function, in panel **(k)**. The resampled, convolved visibility is shown in panel **(n)**. These are the data that the FFT actually sees. The FT of this is the image shown in panel **(m)**; it has been replicated at the various points shown in panel **(k)**. Notice that aliases of the outermost point sources appear just outside the positions of the innermost point sources. This aliasing occurs because the resampling function, shown in panel **(l)**, undersamples (i.e., takes fewer than 2 samples per cycle) of the transform of the outermost point sources. The final operation is correcting for the effect of the convolution. This is done by dividing the image by the Fourier transform of the convolution function. For this example, only the region of the image where the inner lobe of $c > .1$ has been retained, though this is not an issue in practice. The result is shown in panel **(o)**. This is the end product, the 'dirty image' that is supplied to the deconvolution programs.

© Astronomical Society of the Pacific • Provided by the NASA Astrophysics Data System

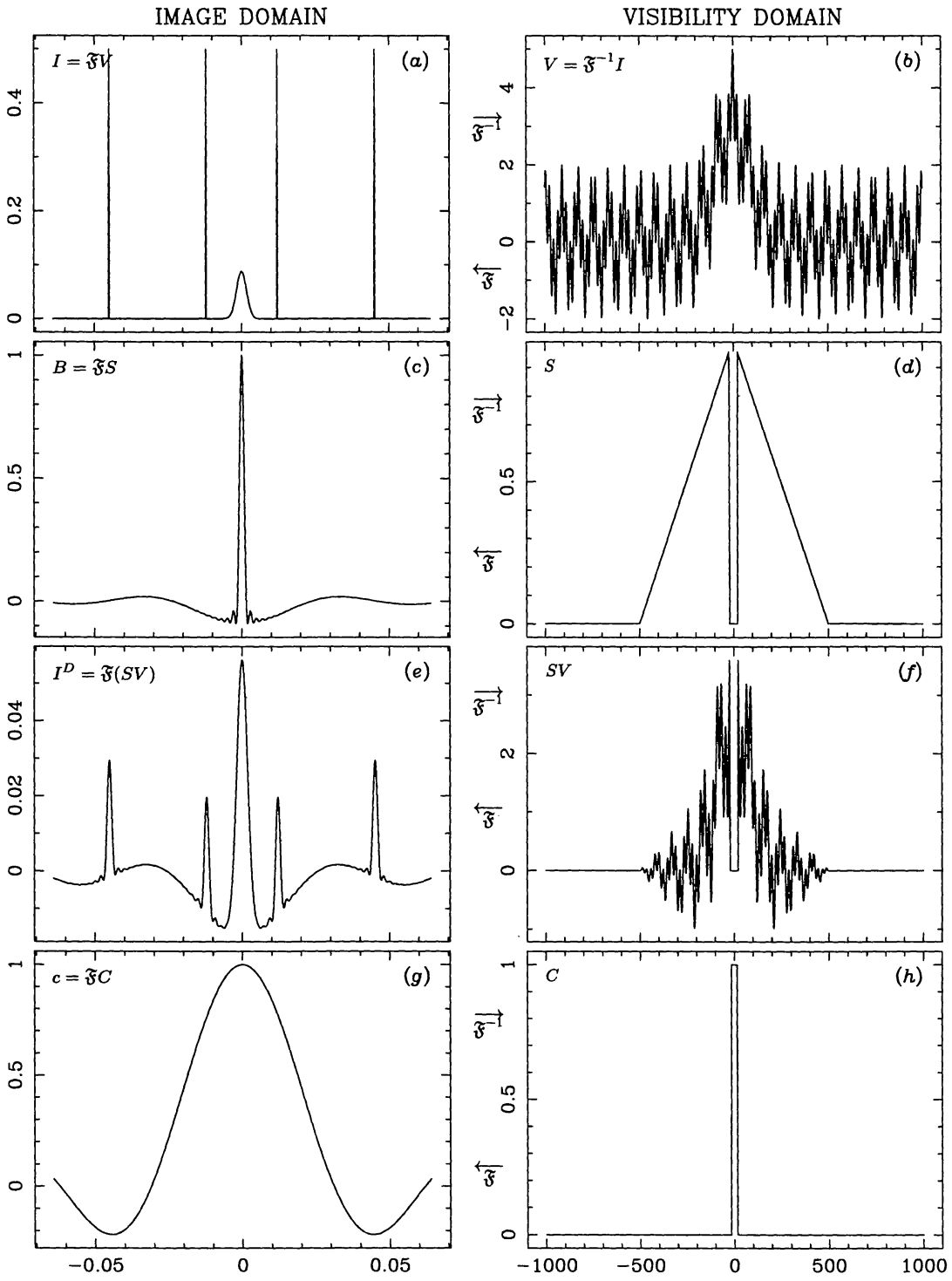

Figure 7–5. *(Caption is on p. 139).* (Continued on next page).

© Astronomical Society of the Pacific • Provided by the NASA Astrophysics Data System

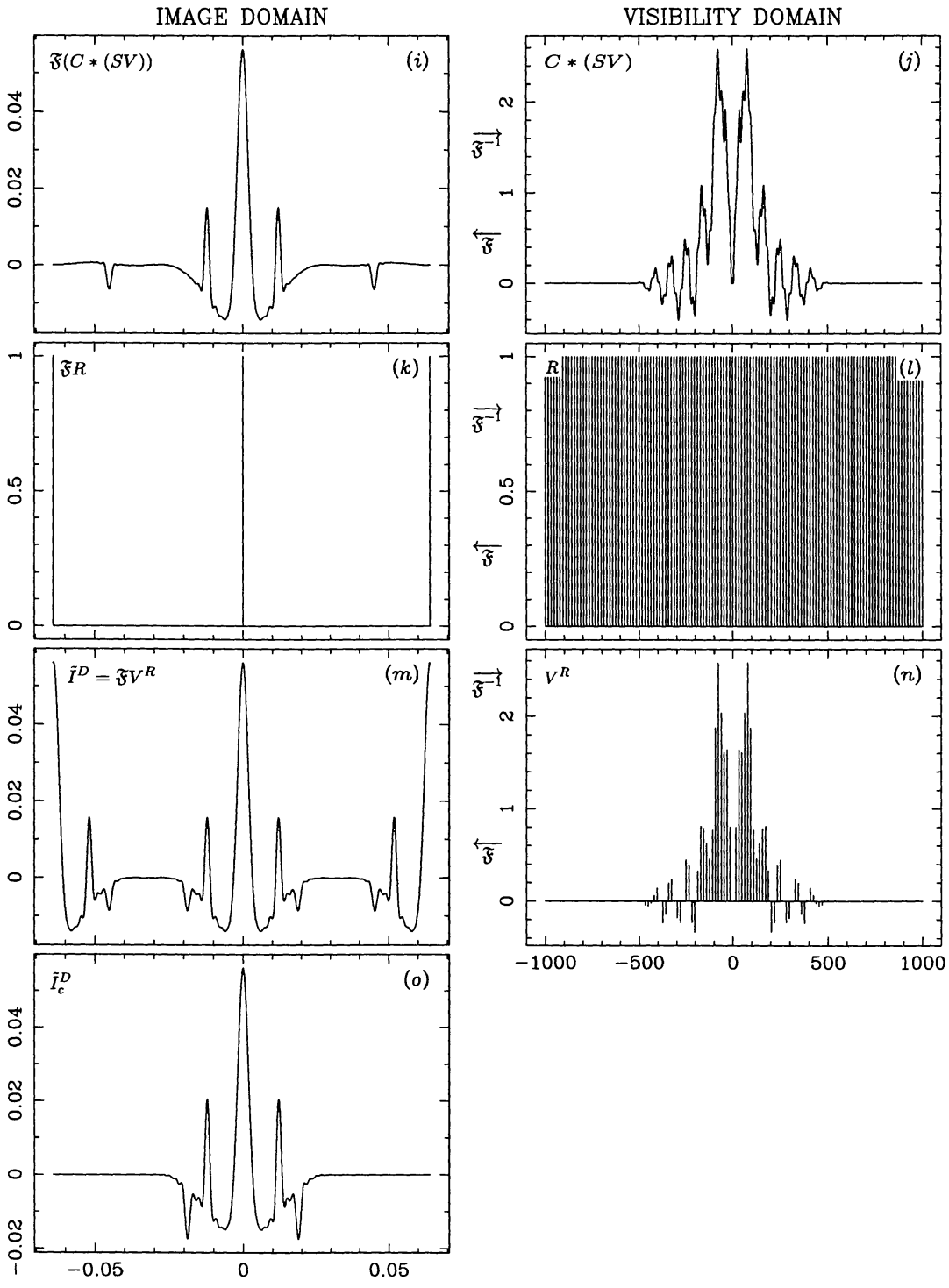

Figure 7–5. *(Continued).*

© Astronomical Society of the Pacific • Provided by the NASA Astrophysics Data System

3.2. Aliasing

Due to the presence of $\mathfrak{F}R$ in Equation 7–16 and to the fact that c is not identically zero outside the primary field of view, parts of the sky brightness that lie outside P are aliased, or 'folded back', into P. Undersampling, and the truncation of the sampling at the boundaries of the (u, v) coverage, are the root causes of aliasing. (If the sky brightness I has features extending over a region of width Ω_l in l and width Ω_m in m, then its visibility function has been undersampled if the visibility samples are separated by more than $1/\Omega_l$ in u and $1/\Omega_m$ in v.) The amplitude of an aliased response from position (l, m) is determined by $|c(l, m)|$. The simplest way to tell whether a feature is aliased or authentic is to calculate images with different cell sizes $\Delta\theta$; an aliased feature then appears to move, while a real one stays the same angular distance from the image center. Additionally, an image covering the full main lobe of the primary beam may quickly reveal whether there is an aliasing problem in an image of a smaller region.

Aliasing of sources that lie outside the primary field of view is only part of the problem. Although it may be possible to obtain visibility samples that are closely enough spaced to avoid undersampling over the sampled region of the (u, v) plane, the finite physical size of the array sets a limit on how far the sampling can extend. For this reason, any authentic feature within P has sidelobes extending outside the image. These sidelobes are also aliased into P, effectively raising the background variance and resulting in a beam shape that depends on position. If, for example, the visibility function is well sampled over a square region of the (u, v) plane but no samples are obtained outside that region, then (assuming uniform weighting) the sidelobes in I^D are precisely those of Gibbs' phenomenon, discussed in Lecture 4.

3.3. Choice of a gridding convolution function

The best ways to avoid aliasing problems are (a) to make the image large enough that there are no sources of interest near the edges of the image, (b) to avoid undersampling, and (c) to use a gridding convolution function C whose Fourier transform c drops off very rapidly beyond the edge of the image. Desideratum (c) favors gridding convolution functions that are not highly confined in the (u, v) plane. But, in practice, computing time restricts one's choice of C to functions that vanish outside a small region, typically six or eight (u, v) grid cells across. A compromise must be struck between alias rejection and computing time. Most programs to date have used a width of six cells, though the modern trend may be moving towards eight.

C is always taken to be real and even. And, since C is usually separable—i.e., $C(u, v) = C_1(u)C_2(v)$—we shall continue the discussion in just one dimension. Typical choices for C are:

- a 'pillbox' function,
- a truncated exponential,
- a truncated sinc function ($\operatorname{sinc} x \equiv \frac{\sin \pi x}{\pi x}$),
- an exponential multiplied by a truncated sinc function, and

© Astronomical Society of the Pacific • Provided by the NASA Astrophysics Data System

- a truncated spheroidal function.

Each is truncated to an interval of width m grid cells, so that $C(u) \equiv 0$ for $|u| > m\Delta u/2$; thus $\mathcal{O}(Mm^2)$ arithmetic operations are required for gridding. These functions are described below; for more discussion see Schwab (1978, 1980):

- *Pillbox.* $C(u) = \begin{cases} 1, & |u| < m\Delta u/2, \\ 0, & \text{otherwise}. \end{cases}$ For $m = 1$, convolution with this C is equivalent to simply summing the data in each cell. Calculation of these sums is fast, but the alias rejection is the worst of the five functions considered here. c is a scaled sinc function.

- *Exponential.* $C(u) = \exp\left[-\left(\frac{|u|}{w\Delta u}\right)^{\alpha}\right]$. Typically $m = 6$, $w = 1$, and $\alpha = 2$. That is, a truncated Gaussian is often used, in which case c can be expressed in terms of the error function.

- *Sinc.* $C(u) = \operatorname{sinc}\frac{u}{w\Delta u}$. Typically $m = 6$, $w = 1$. c can be expressed in terms of the sine integral. If m is allowed to increase, c approaches a step function that is constant over P and zero outside. This is the intuitive justification for considering the use of this function, that the FT of a unit step function truncated at $\pm\frac{1}{2}$ is the sinc function.

- *Exponential times sinc.* $C(u) = \exp\left[-\left(\frac{|u|}{w_1\Delta u}\right)^{\alpha}\right] \operatorname{sinc}\frac{u}{w_2\Delta u}$. Typically[7] $m = 6$, $w_1 = 2.52$, $w_2 = 1.55$, $\alpha = 2$; i.e., a truncated, Gaussian-tapered sinc function is often used. c can easily be computed by numerical quadrature, but it lacks a closed-form expression.

- *Spheroidal functions.* $C(u) = |1 - \eta^2(u)|^{\alpha}\psi_{\alpha 0}(\pi m/2, \eta(u))$, with $\psi_{\alpha 0}$ a 0-order spheroidal function (Stratton 1935), $\eta(u) = 2u/m\Delta u$, and $\alpha > -1$. For $\alpha = 0$ this is the 0-order 'prolate spheroidal wave function', which is the optimal C (among all square-integrable functions of width m grid cells) in that the energy concentration ratio $\int_P |c(l)|^2\,dl \,/ \int_{-\infty}^{\infty} |c(l)|^2\,dl$ is maximized. The other $\psi_{\alpha 0}$ are optimal in the sense of maximizing a *weighted* concentration ratio: for given α, $\int_P w(l)|c(l)|^2\,dl \,/ \int_{-\infty}^{\infty} w(l)|c(l)|^2\,dl$ is maximized, where $w(l) = |1 - 2l\Delta u|^{\alpha}$. Choosing $\alpha > 0$ gives higher alias rejection near the center of the image, at the expense of alias rejection near the edges. ψ_{00} is its own FT, in the sense that if you truncate it as done here, and then take the FT, what you get back is ψ_{00}. Similarly, the other $\psi_{\alpha 0}$ are finite Fourier self-transforms, in the sense that if you so truncate one, weight it, and transform it, what you get back is $\psi_{\alpha 0}$. $\psi_{\alpha 0}$ is used at the VLA, with $m = 6$ and $\alpha = 1$ being typical. See Schwab (1984) for further discussion and additional references.

[7]For a gridding convolution function of this particular parametric form, these values of the characteristic widths w_1 and w_2 are an optimal choice, in the sense described below in the discussion of ψ_{00}.

© Astronomical Society of the Pacific • Provided by the NASA Astrophysics Data System

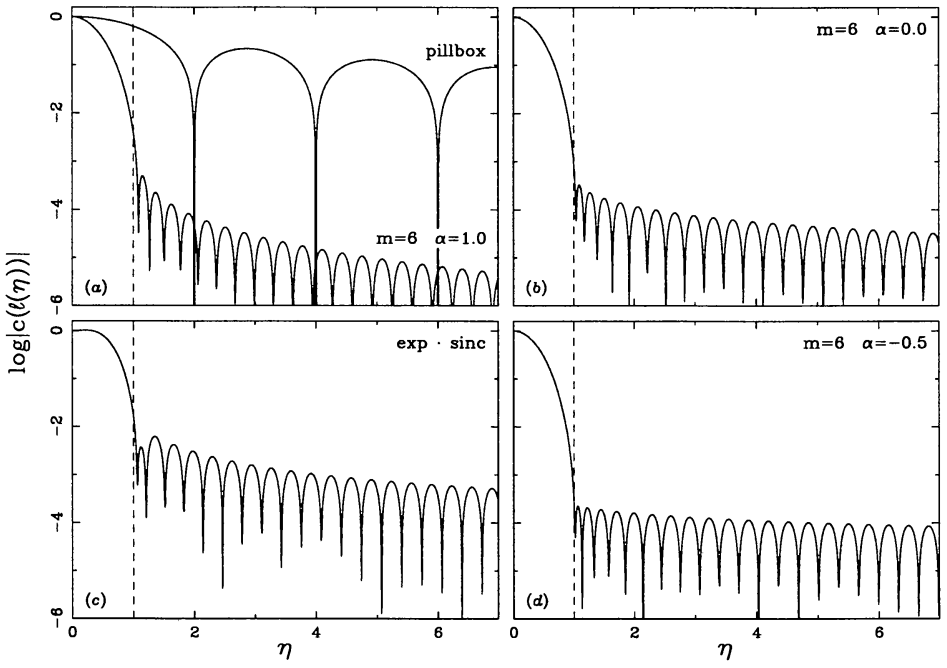

Figure 7–6. For some typical gridding convolution functions C, plots of the absolute value of the Fourier transform of C. **(a)** The spheroidal function ψ_{10}, for $m = 6$, compared with the pillbox function ($m = 1$); **(b)** the 'prolate spheroidal wave function' ψ_{00}, $m = 6$; **(c)** an optimized Gaussian-tapered sinc function, $m = 6$; **(d)** the spheroidal function $\psi_{-\frac{1}{2},0}$, $m = 6$. Panel **(a)** is comparing the function most commonly used at the VLA with the simple but particularly poor choice of a pillbox. Adapted from Schwab (1984).

Figure 7–6 shows the Fourier transforms of various typical gridding convolution functions, normalized to unity at $l = 0$. The abscissa on this plot is in units of image half-widths, $\eta = 2l\Delta u$, so that $\eta = \pm 1$ at the image edges. The image response is suppressed at the edge for both functions, however the exp · sinc function is flatter inside P, and drops much faster past the image edge. The aliased response can, of course, be negative, producing an apparent 'hole' in the image.

The plots in Figure 7–6 compare the pillbox function and the Gaussian-tapered sinc function with several spheroidal functions. The quantity of most direct importance is the ratio of the intensity of an aliased response to the intensity the feature would have if it actually lay within the primary field of view P, at the position of its alias: if η' denotes the position within P at which the aliased response of a source at position η appears, then this suppression ratio is given by $q(\eta) = |c(l(\eta))/c(l(\eta'))|$. (And η' is given by $\eta' = ((\eta+1) \bmod 2) - 1$; it is useful to sketch a plot to convince oneself of this.) The suppression ratio for the same functions as in Figure 7–6 is given in Figure 7–7.

The pillbox, exponential, and sinc functions do not give as effective alias rejection as the exp · sinc or the spheroidal. The exp · sinc has somewhat smaller corrections and, thus smaller errors (due to round-off noise and to violation of the assumptions that make the grid correction valid), near the image edges, while the spheroidal has better rejection beyond the image edge (Schwab 1984).

© Astronomical Society of the Pacific • Provided by the NASA Astrophysics Data System

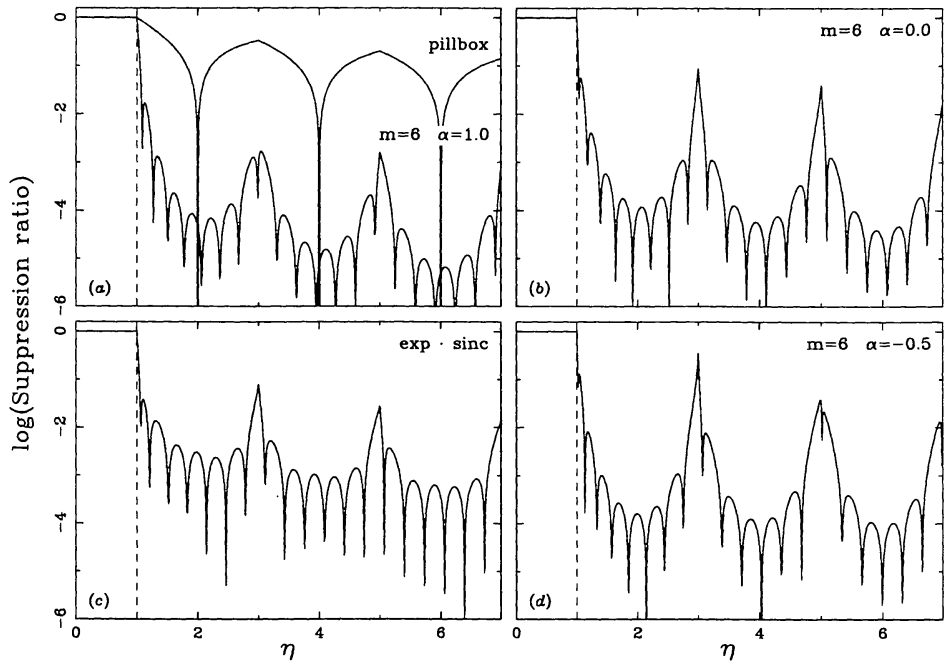

Figure 7–7. The suppression ratio for the same convolution functions as in Figure 7–6.

Remember that the convolution functions suppress only aliased responses. Sidelobes which legitimately fall within the primary field of view, whether from sources inside or outside P, are not suppressed (see Fig. 7–8). With alias suppression of 10^2 to 10^3, at two or three image half-widths, it is these sidelobes which may cause the dominant spurious image features and impair effective deconvolution.

4. Additional Topics

4.1. Translating, rotating, and stretching images

The Fourier transform possesses three basic symmetry properties that are useful in radio interferometric imaging. The first important property is the behavior of the Fourier transform with respect to translation—that is, with respect to a shift of origin: namely, if you shift a function, i.e., replace $f(\mathbf{u})$ by $f(\mathbf{u} - \Delta\mathbf{u})$, and take the FT you get the same result as if you had first taken the FT and then multiplied by $e^{2\pi i \mathbf{x}\cdot\Delta\mathbf{u}}$ (here $\mathbf{x}$ denotes the variable in the transform domain). Similarly, if you want a shift of origin $\Delta\mathbf{x}$ in the transform domain, all you need do is multiply, before transforming, by a factor $e^{-2\pi i \mathbf{u}\cdot\Delta\mathbf{x}}$. Thus, in imaging, all that is required to achieve a shift of origin in the image is to multiply the visibilities by the appropriate complex exponentials before transforming.

The second important property is that the Fourier transform commutes with rotations; that is, if you take the FT and then rotate the coordinate system in the transform domain, you get the same result as if you had first rotated the coordinate system and then taken the FT. Thus, to 'turn an image around', all that you need do is rotate the (u, v) coordinates of the visibility data. (It is easy

© Astronomical Society of the Pacific • Provided by the NASA Astrophysics Data System

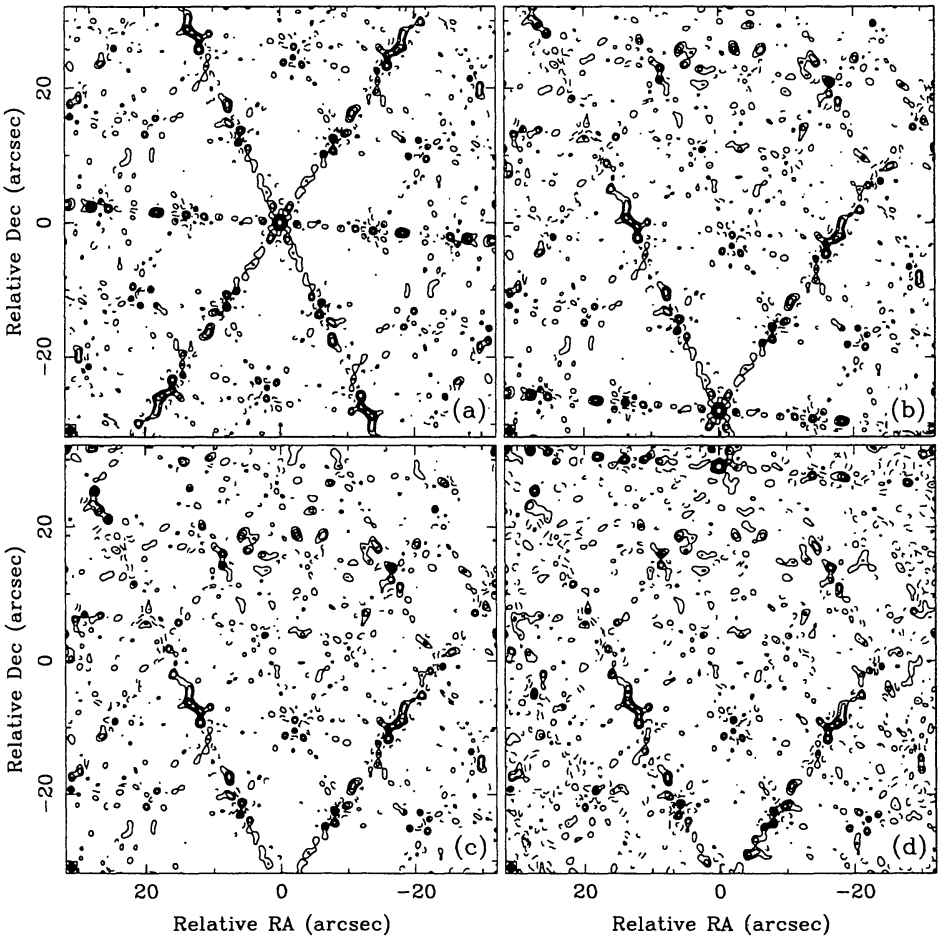

Figure 7–8. The effects of aliasing: **(a)** a point source at the field center using the standard spheroidal convolution; **(b)** the same source near the image edge; **(c)** the same source below the image edge—the sidelobe response is unchanged, but there is no obvious aliased response to the source; **(d)** the source below the lower image edge, but using the pillbox convolution function—a dramatic aliased image of the source appears at the top edge.

to see why the FT has this property: the inner product $\mathbf{u} \cdot \mathbf{x}$ in the exponential kernel of the FT is invariant under rotation.) At the VLA, the visibility (u, v) coordinates are routinely rotated to correct the data for differential precession—i.e., to put the data into the coordinate reference frame of a standard epoch, say, J1950 or J2000. Data taken at two different epochs, say a year apart, need this correction for differential precession before they can be sensibly combined or compared; routine correction to a standard epoch automatically rectifies this problem. Additionally, it is sometimes convenient to rotate the coordinate system so that features in a source have a particular alignment in an image. For an elongated source, this can reduce the data storage requirements (by reducing the number of pixels needed to represent the source by a computed, discrete image) and therefore aid during deconvolution (see Lecture 8) by reducing the required number of arithmetic operations.

The third basic symmetry property of the FT is that it *anti*-commutes with dilations. That is, if you 'stretch' a function linearly and isotropically, then

© Astronomical Society of the Pacific • Provided by the NASA Astrophysics Data System

its FT 'shrinks' proportionately. (That is, the FT of $g(\mathbf{u}) = f(\alpha\mathbf{u})$ is given by $(\mathfrak{F}g)(\mathbf{x}) = \alpha^{-n}(\mathfrak{F}f)(\mathbf{x}/\alpha)$. The multiplicative constant α^{-n} depends on the dimensionality n.) Or, if you linearly stretch a function in just one coordinate, then its FT 'shrinks' proportionately, but in only one of the coordinate directions. This property is the reason that, for a fixed array geometry, the spatial resolution increases (i.e., the characteristic width of the synthesized beam beam decreases) with observing frequency — as the (u, v) coverage expands, the beam shrinks proportionately.

Following Bracewell (1978), the shift property is sometimes called the *shift theorem*, and the dilation property the *similarity theorem*.

4.2. Practical details of implementation

Many Fourier transform imaging programs do not work quite as described above. Sometimes the tapering, introduced in Equation 7–8, and specified by $T(u, v)$, is applied after gridding. This would appear to make only a minute difference. But, in the same sense in which it is incorrect to ignore resampling to justify the grid correction, it is also incorrect to ignore the convolution with $\mathfrak{F}T$, which, if inserted into Equation 7–16, would now appear outside the square brackets.

For economy, Fourier transform imaging programs often do not attempt to evaluate the gridding convolution function very accurately, but instead use a step function (tabular) approximation, with steps spaced at increments of, typically, $\Delta u/100$. This introduces another (not very serious) 'replication' effect like that due to $\mathfrak{F}R$, but one with a very long period, $100/\Delta u$. The grid correction given by Equation 7–18 should be based now on the FT of the step function approximation to C rather than on the FT of C itself. For analysis, see Greisen (1979). (Schwab (1984) gives cheap and accurate rational approximations to the spheroidal functions; the step function approximation is unnecessary.)

4.3. Non-coplanar baselines

In Equation 7–1 the visibility samples are expressed as a function of two variables, u and v, rather than as a function of (u, v, w). As shown in Section 6 of Lecture 2, Equation 7–1 is strictly valid whenever the visibility measurements are confined to a plane, as they would be if obtained with an interferometer array whose elements are aligned along an East–West line; and, again as shown in Lecture 2, this relation is approximately valid when $I(l, m)$ is confined to a small region of sky—that is, when our condition (b) holds, $|w(l^2 + m^2)| \ll 1$. In wide-field imaging with non-coplanar baselines, condition (b) is often violated.

Recall from Lecture 2 (Eq. 2–21) the relation

$$V(u,v,w) = \int_{-\infty}^{\infty}\int_{-\infty}^{\infty} \frac{\mathcal{A}(l,m)I(l,m)}{\sqrt{1-l^2-m^2}} e^{-2\pi i\left(ul+vm+w\left(\sqrt{1-l^2-m^2}-1\right)\right)}\, dl\, dm\,. \quad (7\text{–}21)$$

This can be rewritten as

$$V(u,v,w)e^{-2\pi iw} = \quad (7\text{–}22)$$
$$\int_{-\infty}^{\infty}\int_{-\infty}^{\infty}\int_{-\infty}^{\infty} \frac{\mathcal{A}(l,m)I(l,m)}{\sqrt{1-l^2-m^2}}\, \delta(n-\sqrt{1-l^2-m^2}) e^{-2\pi i(ul+vm+wn)}\, dl\, dm\, dn\,.$$

© Astronomical Society of the Pacific • Provided by the NASA Astrophysics Data System

Now, by sampling V, weighting by $e^{-2\pi iw}$ and the Fourier kernel, and integrating over (u, v, w), one obtains an analog of Equation 7–2,

$$I^{D\,(3)}(l, m, n) = \int_{-\infty}^{\infty}\int_{-\infty}^{\infty}\int_{-\infty}^{\infty} S(u, v, w)V(u, v, w)e^{-2\pi iw}e^{2\pi i(ul+vm+wn)}\,du\,dv\,dw\,. \tag{7–23}$$

This is equal to a familiar looking three-dimensional convolution:

$$I^{D\,(3)} = I^{(3)} * B^{D\,(3)} \tag{7–24}$$

with

$$I^{(3)}(l, m, n) \equiv \frac{\mathcal{A}(l, m)I(l, m)}{\sqrt{1 - l^2 - m^2}}\,\delta(n - \sqrt{1 - l^2 - m^2})\,, \tag{7–25}$$

and

$$B^{D\,(3)}(l, m, n) \equiv \int_{-\infty}^{\infty}\int_{-\infty}^{\infty}\int_{-\infty}^{\infty} S(u, v, w)e^{2\pi i(ul+vm+wn)}\,du\,dv\,dw\,. \tag{7–26}$$

Note that $I^{(3)}$ is a distribution confined to the celestial sphere embedded in a three dimensional volume and that $B^{D\,(3)}$ is mostly concentrated near the origin, i.e., near $l = m = n = 0$.

Either of the methods described earlier for approximating I^D can be extended straightforwardly to Equation 7–23. In applying the 'direct Fourier transform' method, one simply uses a discrete summation, in analog to Eq. 7–3. In the FFT method, w-terms need to be inserted into Eq. 7–13, defining the gridding operation; a 3–D FFT yields a three-dimensional discretely sampled image[8]; and one interpolates this result to obtain data over a spherical cap, a portion of the surface $(l, m, \sqrt{1 - l^2 - m^2})$. Because usually the importance of the curvature effect is minor and the data cover a small range of w, N_n, the number of slices required in the w- and n-dimensions, is small—typically eight to sixteen. The three dimensional imaging problem will be examined later in more detail in Lecture 19.

4.4. The Problem with I^D —Sidelobes

An astronomer is seldom satisfied with the approximation to I defined by I^D, or with the computed version thereof, $\widetilde{I}_c^D$. This is because of the sidelobes which contaminate I^D. As you have seen, these are due to the finite extent of the (u, v) coverage and to gaps in the coverage. Sidelobes from bright features within an image are likely to obscure any fainter features. The process described

[8]In the FFT method, one normally would want a shift of origin, in order to get the plane tangent to the celestial sphere at $(0, 0, 1)$ shifted to the origin of the third coordinate axis of the grid. This involves multiplying the data by $e^{2\pi iw}$, which cancels the multiplication by $e^{-2\pi iw}$ in Equation 7–23.

© Astronomical Society of the Pacific • Provided by the NASA Astrophysics Data System

here is usually just the first step in obtaining a better approximation to I. Because the convolution relation $\widetilde{I}_c^D = \widetilde{B}_c^D * I$, is approximately valid, this first step provides a starting point for the deconvolution (i.e., sidelobe removal) process described in Lecture 8. However, in cases of very low signal-to-noise ratio (as might occur in an observation to determine the detectability of a putative source) one would often choose not to proceed any further. This is often the case in spectral line observing, where narrow bandwidths lead to low signal-to-noise ratios. With modern computers it is very rare to avoid deconvolution for reasons of computational capacity alone. Basic deconvolution will be described in Lecture 8, with the necessary extensions for 3–D imaging, mosaicing and multi-frequency synthesis in Lectures 19-21.

Acknowledgments. We would like to thank Alan Bridle and Rick Perley for numerous helpful discussions during the preparation of this lecture. Rick Perley kindly provided the original version of Figure 7–5.

References

Briggs, D. S. 1995, *High Fidelity Deconvolution of Moderately Resolved Sources*. Ph. D. thesis, New Mexico Institute of Mining and Technology. Available via `http://www.aoc.nrao.edu/ftp/dissertations/dbriggs/diss.html`

Bracewell, R. N. 1978, *The Fourier Transform and Its Applications*, Second Edition, McGraw–Hill, New York.

Dym, H. & McKean, H. P. 1972, *Fourier Series and Integrals*, Academic Press, New York.

Erickson, W. C., Mahoney, M. J., & Erb, K. 1982, *ApJS*, 50, 403–420.

Greisen, E. W. 1979, VLA Scientific Memorandum No. 131, NRAO.

Schwab, F. R. 1978, VLA Scientific Memorandum No. 129, NRAO.

Schwab, F. R. 1980, VLA Scientific Memorandum No. 132, NRAO.

Schwab, F. R. 1984, in *Indirect Imaging*, J. A. Roberts, Ed., Cambridge University Press (Cambridge, England), pp. 333–346.

Stratton, J. A. 1935, *Proc. Nat. Acad. Sci. U.S.A.*, 21, 51–56.

Thompson, A. R. & Bracewell, R. N. 1974, *AJ*, 79, 11–24.

© Astronomical Society of the Pacific • Provided by the NASA Astrophysics Data System